



# COMMUNICATIONS PHYSICS

## REVIEW ARTICLE

<https://doi.org/10.1038/s42005-018-0094-4>

OPEN

## Topological sound

Xiujuan Zhang<sup>1</sup>, Meng Xiao<sup>2</sup>, Ying Cheng<sup>3</sup>,  
Ming-Hui Lu<sup>1</sup> & Johan Christensen<sup>4</sup>

Recently, we witnessed a tremendous effort to conquer the realm of acoustics as a possible playground to test with topologically protected sound wave propagation. In this article, we review the latest efforts to explore with sound waves topological states of quantum matter in two- and three-dimensional systems where we discuss how spin and valley degrees of freedom appear as highly novel ingredients to tailor the flow of sound in the form of one-way edge modes and defect-immune protected acoustic waves. Both from a theoretical stand point and based on contemporary experimental verifications, we summarize the latest advancements of the flourishing research frontier on topological sound.

In condensed-matter physics, the distinctive phases of matter are characterized by their underlying symmetries that are spontaneously broken. In other words, two phases that cannot be smoothly connected by any path in parameter space have difference in their symmetry properties<sup>1</sup>. For example, the crystal solid ice differentiates itself from the liquid water by breaking the translation symmetry. Using such a way to classify the phases of matter remains a recurring theme until the discovery of the quantum Hall effect (QHE)<sup>2</sup>. In 1980, Von Klitzing found that a two-dimensional (2D) electron gas sample, subjected to low temperature and strong magnetic field, has a quantized Hall conductance, which is independent of sample size and immune to impurities. It was later demonstrated that the state responsible for such phenomena is characterized by a completely different classification paradigm based on the notion of topological order<sup>3,4</sup>, which describes phases of matter beyond the symmetry breaking (that means two different phases can have the same symmetry), therefore opening a new research branch.

The topological description on phases of matter concerns the fundamental properties of the system that are insensitive to continuous perturbations of material parameters and change only under a quantum phase transition. For the QHE, the Hall conductance is such a fundamental property. Its quantization originates from the non-trivial topological properties of the energy bands, which are featured with a non-zero topological invariant, the Chern number, according to the Thouless-Kohmoto-Nightingale-den Nijs (TKNN) theory<sup>4</sup>. The Chern number characterizes the geometric phase (commonly known as the Berry phase<sup>5</sup>) accumulation over the Brillouin zone, and thus is closely related with the behaviors of the energy bands in the

<sup>1</sup>National Laboratory of Solid State Microstructures and Department of Materials Science and Engineering, Nanjing University, Nanjing 210093, China.

<sup>2</sup>Department of Electrical Engineering, and Ginzton Laboratory, Stanford University, Stanford, CA 94305, USA. <sup>3</sup>Key Laboratory of Modern Acoustics, Department of Physics and Collaborative Innovation Center of Advanced Microstructures, Nanjing University, Nanjing 210093, China. <sup>4</sup>Department of Physics, Universidad Carlos III de Madrid, ES-28916 Leganès, Madrid, Spain. Correspondence and requests for materials should be addressed to M.-H.L. (email: [luminghui@nju.edu.cn](mailto:luminghui@nju.edu.cn)) or to J.C. (email: [johan.christensen@uc3m.es](mailto:johan.christensen@uc3m.es))

**Box 1 Schematic illustration of different topological phases**

	Gapped	Gapless	
Topological phases	Normal insulator 	Time-reversal broken QH insulator 	Time-reversal-invariant QSH insulator 
Properties	Normal insulators exhibit band gaps, separating the conducting bands from the valence bands, characterized by the zero Chern number ( $C$ , known as a topological invariant).	By breaking time-reversal symmetry, a quantum Hall (QH) insulator can be realised. It also has a band gap, which is spanned by a gapless edge state, exhibiting an interesting electronic property that is insulating in the bulk but conducting on the edge. This phenomenon is characterized by the non-zero Chern number ( $C$ ).	The inherent spin-orbital coupling of a material can also give rise to non-trivial topological phases, known as the quantum spin Hall (QSH) insulators. They support a pair of gapless edge states emerging in the insulating bandgap. The edge states carry conjugate electronic spins and exhibit spin-dependent propagation behaviors. This is characterized by the spin Chern number ( $C_+$ and $C_-$ ). The total Chern number in this case is zero, implying the time-reversal symmetry is intact.
Topological phases	Time-reversal-invariant QVH insulator 	3D Weyl semimetal 	
Properties	A discrete degree of freedom, namely the valley, has also been proposed to realise a topological state, known as the quantum valley Hall (QVH) insulators. Valley refers to the two energy extrema of the band structure in momentum space, at which the Berry curvature exhibits opposite signs and therefore its integral over the full Brillouin zone is zero, while the integral within each valley is nonzero. As a result, the system shows a valley-selective topologically non-trivial property. The valley Hall effect (VHE) is characterized by valley Chern number ( $C_+$ and $C_-$ ). Total Chern number is also zero, hence the time reversal symmetry is intact.	In parallel with gapped topological phases, topological semimetals, which are featured with topologically protected gapless band structures and accompanied by gapless surface states, have recently emerged as a new frontier. Among them, Weyl semimetals have received particular attention, where the Weyl points (WPs) separated in momentum space carry opposite chiral charges ( $C$ ) and are connected across the domain boundaries by a surface state, i.e., the Fermi arc, upon which the Weyl fermions are robust while carrying currents.	

momentum space. It has been shown that a periodic magnetic flux, which breaks the time-reversal symmetry (unlike the traditional definition of the phases of matter, this symmetry breaking itself does not define the topological order), is able to produce non-zero Chern number<sup>6</sup>. The resulting topologically non-trivial system supports a gapless edge state in the bulk energy gap, exhibiting an interesting electronic property that is insulating in the bulk but conducting on the edge. This is essentially different from a normal insulator, where the Chern number is zero (see Box 1).

Additional to applying a magnetic field, it was quickly found that the inherent spin-orbital coupling of a material can also give rise to non-trivial topological phases<sup>7–12</sup>. Kane and Zhang et al. found in systems with spin-orbital coupling, a pair of gapless edge states emerges in the insulating band gap. The edge states carry conjugate electronic spins and exhibit spin-dependent

propagation behaviors, as sketched in Box 1. This is the so-called quantum spin Hall effect (QSHE). In this case, the total Hall conductance is zero, so is the Chern number, implying the time-reversal symmetry is intact. In fact, it is exactly the time-reversal symmetry that protects the spin-dependent edge states. Though the total Hall conductance is zero, the spin Hall conductance is non-zero and can be described by a  $Z_2$  topological invariant or the spin Chern number<sup>13</sup>.

Recently, another discrete degree of freedom, namely the valley, has also been proposed to realize a topological state, known as the quantum valley Hall effect (QVHE), which is related to valleytronics<sup>14,15</sup>. Valley refers to the two energy extrema of the band structure in momentum space, at which the Berry curvature exhibits opposite signs and therefore its integral over the full Brillouin zone is zero, while the integral within each valley is non-zero. As a result, the system shows a valley-selective topologically

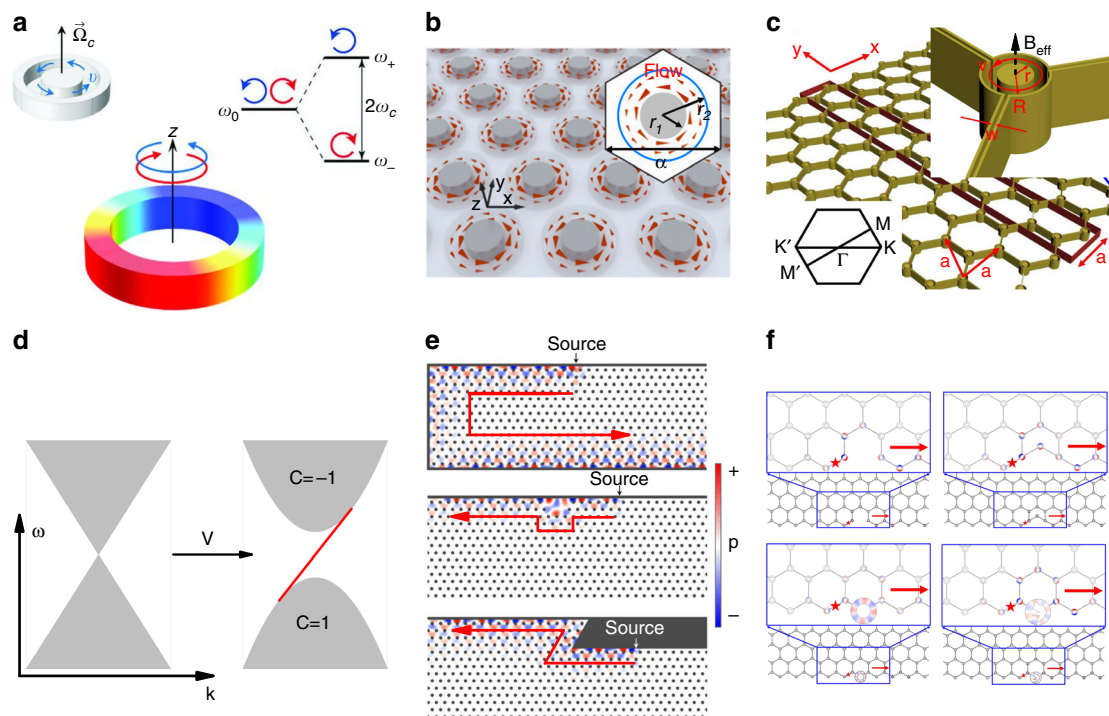


**Fig. 1** Analogue quantum Hall effect in sonic crystals. **a** The airflow-induced acoustic nonreciprocity. In **b, c**, two acoustic quantum Hall lattices incorporated with circulating airflow are presented. **d** Illustration of the band gap opening induced by the airflow, associated with a one-way edge state that spans the bulk gap region. **e, f** The robust edge state propagation against various defects. The figures are adapted from: **a** ref. 21 **b, e** ref. 23 **c, f** ref. 22 (<https://creativecommons.org/licenses/by/3.0/legalcode>)

non-trivial property. It is worth mentioning that the QVHE also maintains intact time-reversal symmetry. Regardless of the nature of abovementioned topological phases, they share the same property that the edge states span the bulk band gap and separate domains with different Chern numbers. In parallel with these gapped topological phases, topological semimetals, which are featured with topologically protected gapless band structures and accompanied by gapless surface states, have recently emerged as a new frontier<sup>16–18</sup>. Among them, Weyl semimetals have received particular attention, as their quasiparticle excitation is the Weyl fermion, which has not yet been observed as a fundamental particle in vacuum. In a Weyl semimetal, the Weyl points separated in momentum space carry opposite chiral charges and are connected across the domain boundaries by a surface state, i.e., the Fermi arc, upon which the Weyl fermions are robust while carrying currents.

The abovementioned topological states and their associated exotic phenomena could promise potential applications in the next generation of electronic devices and topological quantum computing. However, realizing the topological phases poses great challenges that are difficult to overcome in electronic systems, such as the inevitable material defects as well as the validity of the single electron approximation, which is the essential basis of most topological descriptions. Thus, it is not surprising that many of the quantum topological states have been extended to photonic and phononic systems, benefiting from their large scale in both time and space, which makes the control of fabrication and the measurement process much easier and more accurate compared to the electronic systems. Additionally, the photonic/phononic systems are not restricted by the Fermi levels, and therefore any appropriate regions of the spectrum can be of interest. Nevertheless, emulating the topological phases in condensed-matter physics to the classical regime might not be straightforward, due to the key difference between electrons and photons/phonons. For instance, the photons/phonons do not carry a half-integer spin and therefore cannot directly interact with the magnetic

field. Breaking the time-reversal symmetry in these systems requires additional effort. Moreover, the difference between fermions and bosons might also provide new angles to the quest of topological phases of matter, which may have potential applications in the design of low loss photonic/phononic devices. Compared to photonic systems, acoustics differ substantially since longitudinal sound waves lack a transverse polarization degree of freedom that can be used to construct pseudo spins to mimic the spin up and down in electronic systems and breaking the time-reversal symmetry requires additional complexities, both of which are essential in realizing the quantum effects leading to topologically robust sound propagation and involve new physics. This review offers a detailed exposition on some of the recent advancements of the topological states in classical regime, mainly focused on the airborne sound.

The organization of the remainder of this review is as follows. First, we elaborate the main breakthroughs of the analogue QHE and QSHE in acoustics, followed by the development of QVHE. The next section is devoted to the Weyl semimetal. Then, the possibility to extend the topological phases to mechanical waves is discussed. The last section presents our perspectives on possible future directions.

### Analogue quantum Hall effect and quantum spin Hall effect

The QHE provided the first example of the topological phases of matter. Observing the QHE, a 2D sample subjected to low temperature and a strong magnetic field exhibited the behavior of an insulator in the bulk and a metal along the edges where the electrons move unidirectionally without backscattering or dissipation. The associated Hall conductance takes the quantized values of  $\sigma_{xy} = Ce^2/h$ , which are unaffected by impurities. Here,  $h$  represents the Plank constant,  $e$  is the charge of an electron and  $C$  is the Chern number. As mentioned above, it characterizes the topology of the electronic wave functions in the momentum space and is independent on the material properties<sup>3,4</sup>. This is essentially the reason why the QHE is topologically robust against

impurities. For a 2D system, the Chern number can be evaluated by

$$C = \frac{1}{2\pi} \int F(\mathbf{k}) \cdot d\mathbf{s}, \quad (1)$$

where  $F(\mathbf{k}) = \nabla_{\mathbf{k}} \times A(\mathbf{k})$  is defined as the Berry curvature and  $A(\mathbf{k}) = \langle u_n(\mathbf{k}) | i\nabla_{\mathbf{k}} | u_n(\mathbf{k}) \rangle$  is the Berry connection.  $u_n(\mathbf{k})$  represents the periodic part of the Bloch state on the  $n$ th energy band with momentum  $\mathbf{k}$ . Under the symmetry operations, the Berry curvature obeys the rules of  $PF(\mathbf{k}) = F(-\mathbf{k})$  and  $TF(\mathbf{k}) = -F(-\mathbf{k})$ , where  $P$  and  $T$  denote the parity and time-reversal operators, respectively. Note that when the system breaks  $T$  symmetry but preserving the  $P$  symmetry, the integral in Eq. (1) (which runs over the entire Brillouin zone) acquires a non-zero value, so does the Chern number. Non-zero Chern number corresponds to a topological non-trivial phase while zero Chern number corresponds to a topological trivial phase. The topological phases with non-zero Chern number offer intriguing wave transport properties like one-way edge propagation and robustness against impurities, which might have promising applications in the next-generation of electronic devices and quantum computing.

Driven by their development in electronic systems, the topological phases were quickly transferred to the classical realms, with the analogue QHE in photonics firstly proposed and experimentally realized at microwave frequencies<sup>19,20</sup>. The considered system is a 2D photonic crystal, comprising a gyromagnetic material subjected to a magnetic field that breaks the  $T$  symmetry. Consequently, topologically protected edge states were constructed, featured with one-way wave transport behaviors that are robust against defects and bends. In acoustics, however, breaking the  $T$  symmetry is quite challenging, usually involving additional complexities, such as using magneto-acoustic materials or introducing nonlinearity. These possibilities either require large volumes or introduce inherent signal distortion, which are typically impractical. Inspired by the magnetic bias producing electromagnetic nonreciprocity in gyromagnetic materials, Fleury et al. proposed a feasible method to break the  $T$  symmetry in acoustics, relying on moving airflow in ring cavities<sup>21</sup>. The imparted airflow, taking the role of magnetic bias, splits the degeneracy of the two counter-propagating azimuthal resonant modes in the ring cavities, as shown in Fig. 1a, therefore inducing acoustic nonreciprocity. More specifically, consider the following wave equation for sound propagating in a circulating airflow with velocity  $\mathbf{V}$ <sup>22</sup>,

$$[(\nabla - i\mathbf{A}_{\text{eff}})^2 + \omega^2/c^2 + (\nabla\rho/2\rho)^2 - \nabla^2\rho/(2\rho)]\phi = 0, \quad (2)$$

where  $\phi$  is the velocity potential,  $\omega$  is the angular frequency,  $c$  is the sound speed and  $\rho$  is the mass density of air. For non-zero  $\mathbf{V}$ , the term  $\mathbf{A}_{\text{eff}} = -\omega\mathbf{V}/c^2$  gives rise to an effective vector potential, which generates an effective magnetic field  $\mathbf{B}_{\text{eff}} = \nabla \times \mathbf{A}_{\text{eff}}$  that breaks the  $T$  symmetry.

Based on this principle, several designs of analogue QHE in sonic crystals have been reported<sup>22–26</sup>. In Fig. 1b, c, a hexagonal lattice and a honeycomb lattice, respectively, are illustrated as examples. The inset in Fig. 1c illustrates how the effective magnetic field is generated to break the  $T$  symmetry. Due to the intrinsic lattice symmetry, a pair of Dirac-like points deterministically appears at the Brillouin zone boundary for  $\mathbf{V} = 0$ <sup>27–29</sup>, when the airflow is introduced, the Dirac-like degeneracies are lifted as a consequence of the  $T$  symmetry breaking<sup>22,23</sup>. This is characterized by a band gap opening, as illustrated in Fig. 1d. The evaluated Chern number for the bands below and above the opened gap acquires non-zero values ( $C = 1$  for the lower band and  $C = -1$  for the upper band), implying the systems are in the topologically non-trivial phase. According to the principle of the bulk-edge correspondence, a signature of such topologically non-trivial system is the presence of one-way edge states along its boundaries when truncated by other topologically trivial systems

(i.e.,  $C = 0$ ). Correspondingly, acoustic wave propagation exhibits unidirectional behaviors, which are topologically protected and robust against various defects and sharp bends, as demonstrated by Fig. 1e, f.

To experimentally implement the above discussed airflow-based designs, uniformly biased circulators are required, which impose serious challenges, such as nonsynchronous rotation and flow instability. This makes the practical implementation elusive until recently, Zhu et al. proposed a rotating chiral structure based on ring resonators that support high-order whispering gallery modes with high Q factor<sup>30</sup>. This special design allows the system to produce giant acoustic nonreciprocity at small rotation speed, and therefore a stable and uniform airflow can be generated. On the other hand, using active liquids that can flow spontaneously even without an external drive has also been explored to break the  $T$  symmetry<sup>31,32</sup>. This might relax the experimental requirements and bring new opportunities to topological phases of matter in active materials, for which, uniquely inherent material properties like microscopic irreversibility may help to achieve functionalities that are absent using only passive materials.

In addition to the QHE that requires breaking of the  $T$  symmetry, it is naturally interesting to explore topological phases under preserved  $T$  symmetry, i.e., the QSHE, also known as the topological insulators (TIs)<sup>11,12</sup>. The QSHE can be regarded as the effect of two coupled quantum Hall states. Differently, the spin-orbit coupling plays an essential role in the QSHE where the coupling between spin and orbital angular momentum causes the moving electrons to feel a spin-dependent force, even in the absence of magnetic materials. As a result, the electrons with opposite spin angular momenta (often referred as spin up and spin down) will move in opposite directions along the edges. The topological order that characterizes this phenomenon is described by the so-called spin Chern number (or the  $Z_2$  topological invariant), which is defined as<sup>33</sup>

$$C_{\pm} = \frac{1}{2\pi} \int F_{\pm}(\mathbf{k}) \cdot d\mathbf{s}, \quad (3)$$

where  $F_{\pm}(\mathbf{k}) = \nabla_{\mathbf{k}} \times \langle u_{\pm}(\mathbf{k}) | i\nabla_{\mathbf{k}} | u_{\pm}(\mathbf{k}) \rangle$  is the Berry connection, similar as that in Eq. (1). The electron states are unambiguously decomposed into two sectors,  $u_+(\mathbf{k})$  and  $u_-(\mathbf{k})$ , representing the spin up and down components, respectively. The spin Chern numbers defined in Eq. (3) have been proved to be true topological invariants, which are robust against the presence of finite disorder scatterings, including spin nonconserving symmetry-breaking perturbations. In other words, any non-magnetic impurities will not eliminate the metallic edge states, as the electrons are never completely reflected when scattered, even if the impurity becomes stronger and the description with respect to well-separated scattering events is invalid.

The QSHE with edge states that are spin-locked and protected by the  $T$  symmetry also found its counterparts in photonics and phononics, but not straightforward. It is well known that for fermions with half-integer spin, like the electrons, the  $T$  symmetry operator satisfies  $T_f^2 = -1$ , and hence guarantees the Kramers degeneracy, which is crucial for the QSHE<sup>12</sup>. However, for bosons with integer spin, like the photons and phonons, the  $T$  symmetry operator obeys  $T_b^2 = 1$ , which is essentially different from the fermions. Consequently, to realize analogue QSHE in bosonic systems, it is necessary to construct fermion-like pseudo spins and pseudo  $T$  symmetry<sup>34</sup>. In photonics, different polarizations were used to construct pseudo spins as TE + TM/TE – TM (where TE and TM are the transverse electric and magnetic polarizations)<sup>35</sup>, as TE/TM<sup>36</sup> and as left/right circular polarizations<sup>34</sup>. In acoustics, however, due to the lack of various polarizations (sound propagates longitudinally only), it is even more challenging to realize analogue QSHE. A possible solution was addressed based on using coupled resonators that support

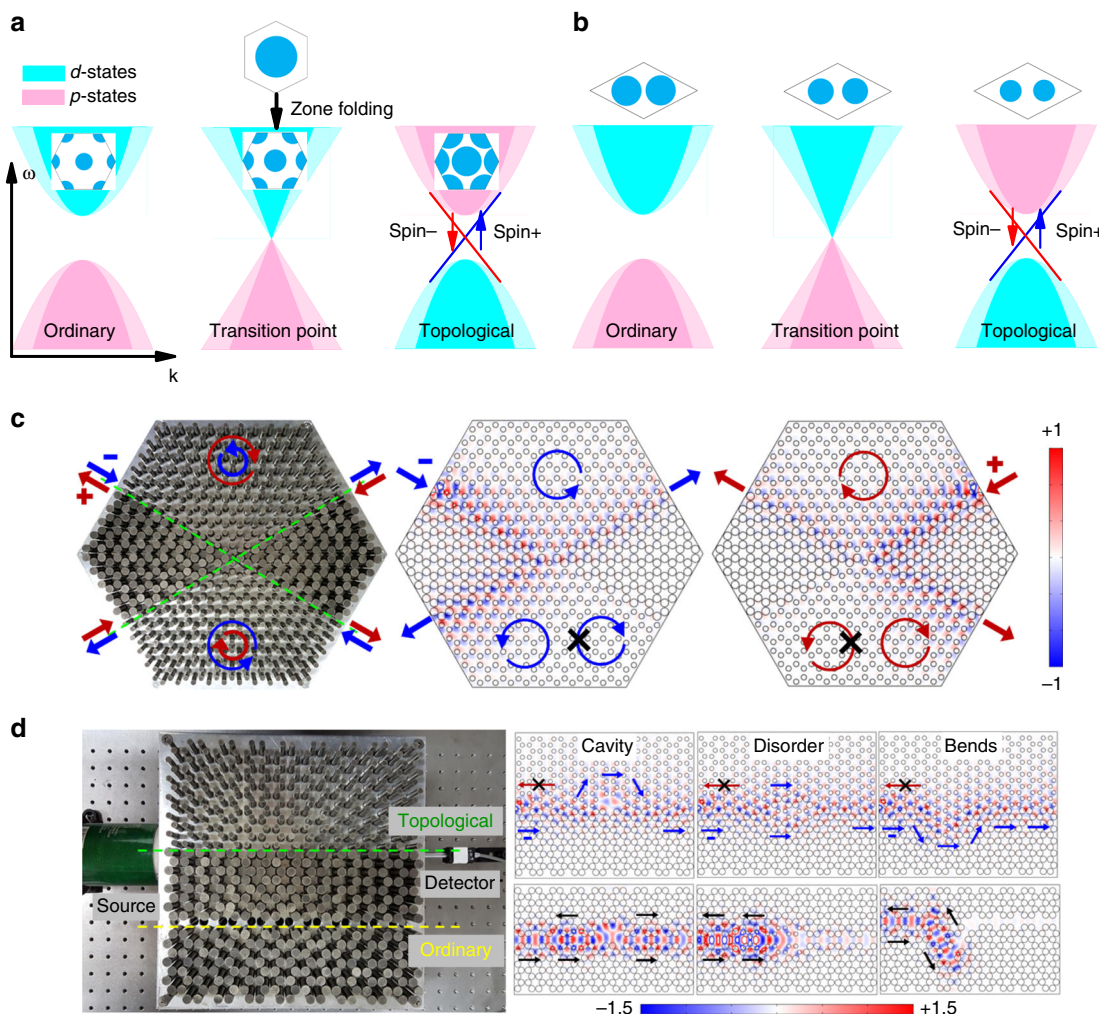


**Fig. 2** Analogue quantum spin Hall effect in sonic crystals. The construction of doubly degenerate Dirac-like cones based on **a** zone folding and **b** accidental degeneracy is presented. **c** The spin-locked edge state propagation and **d** its robustness against various defects. Wave propagation in a regular waveguide is also presented as comparison. Panels **c**, **d** are adapted from ref. <sup>43</sup>

clockwise and anticlockwise resonant modes, which impart the pseudo spins<sup>37,38</sup>. Recently, another approach was proposed utilizing two degenerate Bloch modes, instead of two polarizations or two resonant modes, to create the pseudo spin states<sup>39</sup>. Specifically, by expanding a primitive unit cell to a larger cell, the Dirac-like cones at the  $K$  and  $K'$  points in the original Brillouin zone are folded at the  $\Gamma$  point in the new Brillouin zone, forming the doubly degenerate Dirac-like cones. By tuning the composite material or geometric parameters, a band inversion can happen near the degenerate point, associated with a topological transition (Fig. 2a). The harmonic polarized electromagnetic (EM) modes<sup>39</sup> or the scalar acoustic modes<sup>40,41</sup> exhibit electronic orbital  $p$ -like and  $d$ -like wave shapes, which essentially give the correspondence between the EM or acoustic wave functions with positive and negative angular momenta and the spin-up and down states of the electrons. Later on, an accidental degeneracy technique<sup>42</sup> was also implemented to create the doubly degenerate Dirac-like cones and the pseudo spins<sup>43,44</sup>, taking the advantage of the large index and impedance contrast of the composite materials, which is especially common in acoustics.

Here, we demonstrate in detail how the acoustic analogue QSHE can be realized in a honeycomb lattice consisting of steel rods in air, based on the accidental degeneracy<sup>43</sup>. Due to the 2D irreducible representations of the  $C_{6v}$  symmetry, the honeycomb lattice supports two pairs of degeneracies at the  $\Gamma$  point, the dipolar modes  $p_x/p_y$  and the quadrupolar modes  $d_{x^2-y^2}/d_{xy}$ ,

which can hybridize to emulate the pseudo spins. By decreasing the filling ratio of the steel rods, the two pairs of dipolar and quadrupolar modes, separated by a band gap, will move in frequency and exchange their positions (the so-called band inversion). In between, there is a point where the band gap is closed and the two pairs accidentally touch together, forming the doubly degenerate Dirac-like cones (essentially different from the zone folding mechanism). This gap-opened, closed and re-opened process is sketched in Fig. 2b, which leads to a topological transition from the trivial (ordinary) state to the non-trivial (topological) state. The transition point is exactly the double Dirac-like point. In the topological non-trivial state, a pair of edge states appear, carrying opposite group velocities to emulate the spin-up and down states. Correspondingly, the spin-dependent sound propagation can be expected, which is depicted in Fig. 2c. More studies in Fig. 2d reveal that the spin-locked edge state propagation is immune to various defects, including cavities, disorders, and bends, essentially different from a regular waveguide. It is worth mentioning that as the  $C_{6v}$  symmetry is not perfectly preserved at the interface between the trivial and non-trivial lattices, the two counter-propagating pseudo spin states are slightly mixed and a tiny gap exists at the center of the Brillouin zone. As a result, the backscattering of the edge states is not completely suppressed. Fortunately, by engineering the rod size, this gap can be sufficiently reduced. Recently, the accidental degeneracy technique also spurred the development of topological

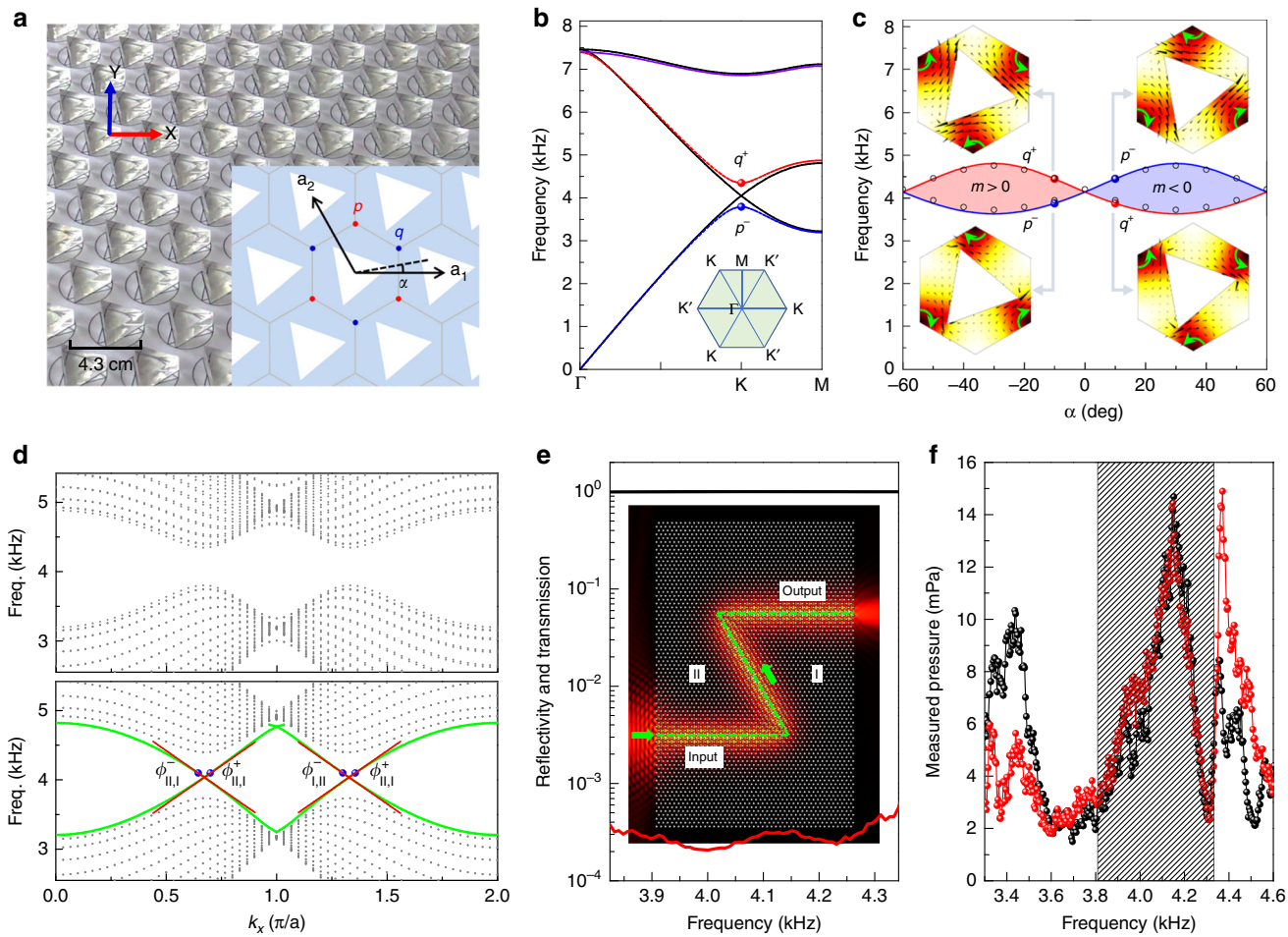


**Fig. 3** An acoustic valley Hall (AVH) insulator, reproduced from ref. 71. **a** A schematic of the sonic crystal, where the inset shows the cross-sectional view. **b** Dispersion relations for the gapless case of  $\alpha = 0^\circ$  (black lines) and gapped cases of  $-10^\circ$  (color lines). **c** Topological phase dependency with  $\alpha$  where the inset shows the vortex features. **d** Dispersions for the interfaces separating two topologically identical (upper panel) and distinct (lower panel) AVH insulating phases. **e** Power transmission (black line) and reflection (red line) spectra for a zigzag path, where the inset shows the field distribution. **f** Transmitted pressure measured for the zigzag path (red circles), and a straight channel (black circles)

phases in the elastic realm, where an elastic analogue QSHE was experimentally demonstrated in a phononic crystal plate with perforated holes<sup>45</sup>. This might have potential applications in chip-scale acoustic devices, such as waveguide and splitter.

#### Acoustic valley-Hall and pseudo spin effect

The discrete valley degree of freedom<sup>15,46–50</sup>, labeling quantum states of energy extrema in momentum space, is attracting rapid growing attention because of its potential as a new type of information carrier like spins in spintronics. Transferring the valley concept to classical wave systems, it has been shown that the existence of valley-like frequency dispersions, engineered in artificial crystals, has been made possible with photonic crystals<sup>51–67</sup> and sonic crystals (SCs)<sup>27,68</sup>. Soon after that, the QVHE<sup>69,70</sup> and corresponding valley-protected edge states<sup>71–77</sup> were theoretically predicted and experimentally observed in two-dimensional acoustic systems.

Lu et al.<sup>69,71</sup> firstly introduced the concept of valley states to SCs for acoustic waves. The hexagonal SC consists of triangular rods in a 2D waveguide, of which symmetries can be characterized by the rotation angle  $\alpha$  (Fig. 3a). It has been pointed out that the existence of a two-fold Dirac degeneracy at the corners of the 1st Brillouin zone (BZ) for any SC with  $\alpha = n\pi/3$  is protected by the  $C_{3v}$  symmetry, whereas the degeneracy would be lifted for any other rod orientation breaking the mirror symmetries<sup>68</sup>. As

shown in Fig. 3b, the dispersion relations for the SCs with  $\alpha = 0^\circ$  and  $-10^\circ$  are illustrated. The vortex revolution at each valley (i.e., clockwise and anticlockwise) plays the role of the valley degree of freedom in a 2D acoustic system, as shown in insets of Fig. 3c. Figure 3c shows the tuning of the acoustic valley-Hall (AVH) phase transition in a SC by variation of the rotating angle  $\alpha$ . When  $\alpha < 0^\circ$ , the vortex chirality of the lower (upper) state is clockwise (anticlockwise), which appears exactly inverted when  $\alpha > 0^\circ$ . The AVH phase transition that is accompanied by the crossing of these two pseudo spin states can be captured by an  $\alpha$ -dependent continuum Hamiltonian. Derived from the  $\mathbf{k} \cdot \mathbf{p}$  theory, the unperturbed Hamiltonian  $\mathcal{H}(k_\perp) \equiv \mathcal{H}_0(\delta k)$  near the Dirac points can be written as<sup>78</sup>  $\mathcal{H}_0(\delta k) = v_D (\delta k_x \sigma_x + \delta k_y \sigma_y)$ , where  $v_D$  is the group velocity,  $\delta k = (\delta k_x, \delta k_y) \equiv k_\perp - k_D$  is the distance from the Dirac points with  $k_D = \pm \frac{4\pi}{3\alpha_0} e_x$  for the  $K$  and  $K'$  points, and  $\sigma_i (i = x, y)$  are Pauli matrices of the vortex pseudo spins. The perturbation matrix is diagonalized:  $\mathcal{H}_P = m v_D^2 \sigma_z$ . Consistent with the above band inversion picture (Fig. 3c), the sign of the effective mass  $m = (\omega_{q^+} - \omega_{q^-}) / 2v_D^2$  characterizes two different AVH insulators separated by the Dirac semi-metal phase with  $m = 0$  in the phase diagram. The massive Dirac Hamiltonian  $\delta H$  produces a nontrivial Berry curvature  $\Omega(\delta k) = (1/2)mv_D(\delta k^2 + m^2v_D^2)^{-3/2}$  in the first band. The time-reversal

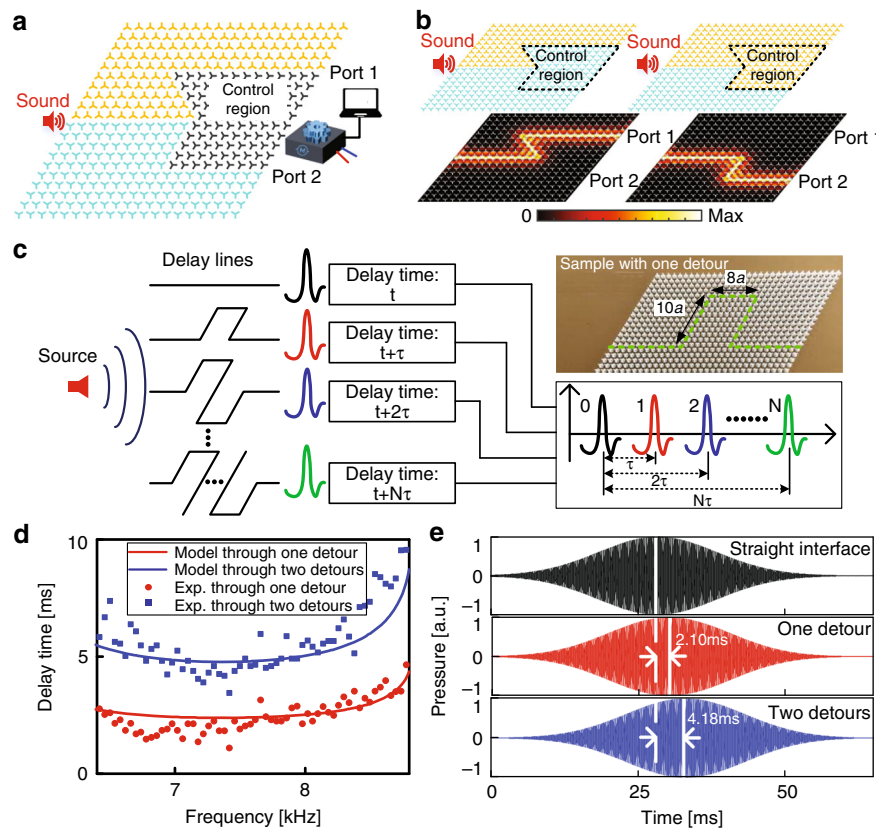


**Fig. 4** Reconfigurable topological switch and broadband topological acoustic delay lines, reproduced from ref. 73. **a, b** Show the setup and the pressure field distributions of the reconfigurable topological switch. **c** Schematic of topological time-delay times. **d, e** Show the time delays and measured signals through one and two detours

symmetry leads to the Chern number  $C = 0$ , which is the integral of Berry curvature over the full BZ. On the contrary, the Berry curvature exhibits strong peaks at the gap minima near  $K$  and  $K'$  points of the BZ for small perturbation  $m$ . The integral of the Berry curvature over an individual valley (one half of the BZ) is accurately defined and the non-vanishing valley-Chern indices can be determined by  $C_K = \text{sgn}(m)/2$ <sup>79</sup>. As a result, the difference in the topological charge across the interface is quantized, which maintains a chiral edge mode according to the bulk-boundary correspondence<sup>79,80</sup>. To verify this, two distinct SC interfaces are studied: one is constructed out of SCs with  $\alpha = 10^\circ$  and  $50^\circ$ , of which the dispersion relation is illustrated in the top panel of Fig. 3d, and the other is constructed out of SCs with  $\alpha = -10^\circ$  and  $10^\circ$ , of which the dispersion relation is shown in the bottom panel. In the former case, the spectrum of relevance is completely gapped due to the presence of identical valley-Hall phases within the facing SCs. However, in the latter case, topological edge states fall within the bulk band gap as indicated by the green lines, which originate from AVH phase-inversion across the interface. Similar to the QSHE, edge states associated to the AVH effect appear robust against bends and crystal defects. Figure 3e shows a negligible weak backscattering of the topological valley-projected edge mode propagating along an interface containing two sharp bends. The experimentally measured pressure amplitudes in the output channel of the interface with and without sharp bends are illustrated in Fig. 3f demonstrating that the transmitted pressure of the edge states with bends almost entirely coincides with the one from a straight path within the topological band gap. Hence, although lattice-scale defects and obstacles may induce inter-valley scattering<sup>73,78</sup> with the suppressed transmission, sharp bends as illustrated in Fig. 3e indicate

that backscattering-immune sound guiding in valley-Hall insulators is readily possible.

As we mentioned earlier, the QVHE enables exciting possibilities using the valley degree of freedom for valleytronics applications. Along the lines of technical implementation, a great challenge is posed by the lack of tunability and adaptation to functional needs concerning the AVH effect. Inspired by the proposal of delay lines in topological photonics<sup>59,62</sup>, Zhang et al.<sup>73</sup> experimentally realized topologically protected broadband delay lines based on engineered phase delay defects (PDDs) that constitute a new platform for acoustic devices. The structure consists of three-legged rods (TLRs) arranged into a triangular lattice providing an enlarged topological band gap through an optimized shape of these rods. The tunability of the unit cell is obtained through computer-controlled motors, which can configure the topologically protected pathway consequently. Sound waves transmit either through Port 1 or Port 2 (see Fig. 4b), depending on the rotation angle selected to be  $-30^\circ$  or  $30^\circ$ , respectively. This configurability of the TLRs to any desired angle further promise vast possibilities of functional devices. Short pulses can transmit through them due to the broadband response character, and their dynamic response can be engineered at will. The tremendous advantage of signal transmission without any reflection even in the pathway with sharp bends enables the acoustic delay lines by means of topologically protected transient edge states. The PDDs in the form of square-shaped detours with four sharp bends along the interface can generate a time delay (see Fig. 4)<sup>62</sup>.

$$\tau_i = \left( \frac{\partial \varphi_i}{\partial \omega} - \frac{\partial \varphi_0}{\partial \omega} \right) = \frac{1}{2\pi} \left( \frac{\partial \varphi_i}{\partial f} - \frac{\partial \varphi_0}{\partial f} \right), (i = 0, 1, 2, \dots, N) \quad (4)$$

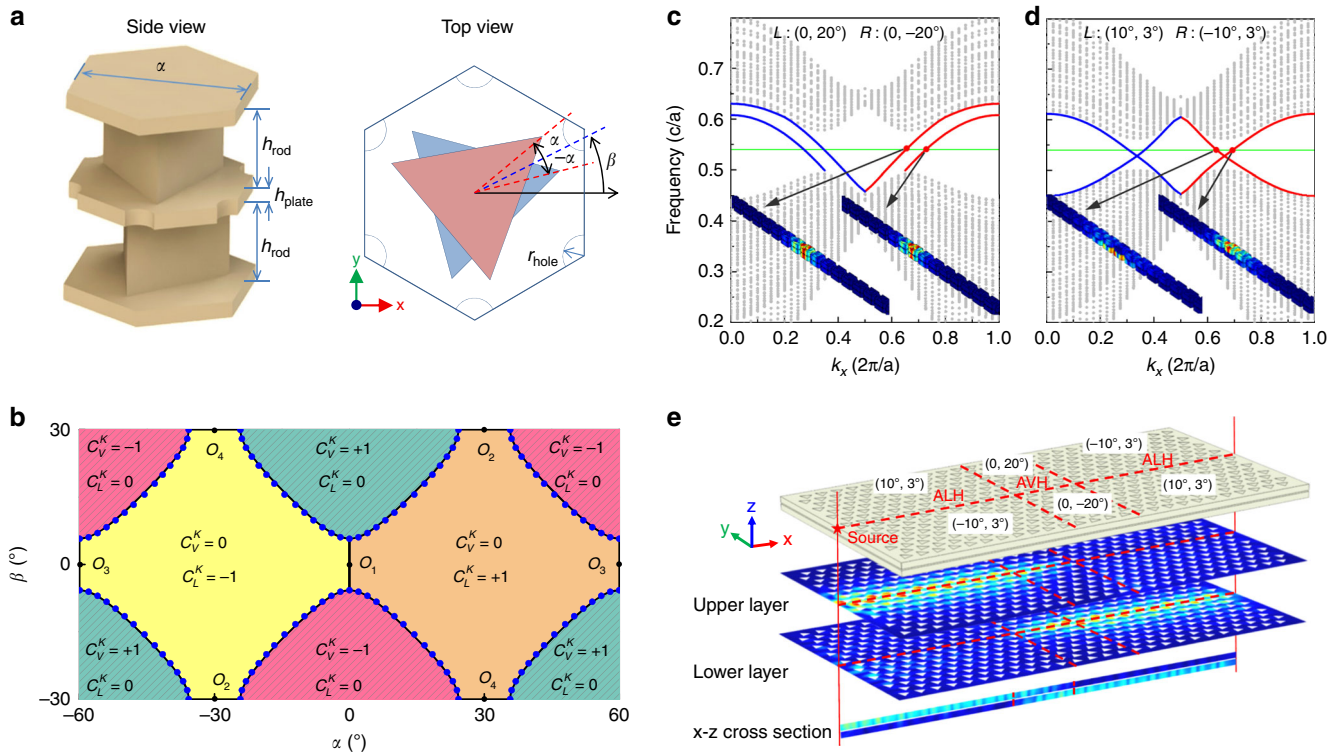


**Fig. 5** Valley topological phase in a bilayer sonic crystal (BSC), adapted from ref. <sup>81</sup>. **a** A schematic of the unit cell, where both the side and top views are shown. **b** Reduced phase diagram in dependence on the angles ( $\alpha, \beta$ ). The numerical phase boundaries (solid lines) confirm the model predictions (dots), which exhibits the closure of the omnidirectional band gap. **c, d** Show the projected dispersion relation along an interface separating two topologically distinct acoustic valley Hall (AVH) BSCs and acoustic layer-valley Hall (ALH) BSCs. **e** Simulated field pattern of sound concentration varying from the upper layer to the lower layer

where  $\partial\varphi_i$  is the phase of the sound wave,  $i$  is the number of detours, and  $\partial\varphi_0$  is the phase through a straight pathway. By stacking multiple detours successively, the time delay can be increased very flexibly. The time delay time  $\tau = \sum_{j=1}^2 \frac{s_j}{c_j}$  can be determined by Eq. (4), where  $s_j$  is the length of the transmitted line,  $c_j = 2\pi (df/dk)_j$  is the sound velocity with  $j = 1, 2$  representing different kind of interfaces. Figure 4d shows the time delays through a single and a double PDD, which is confirmed by the measured signal in Fig. 4e. This design may pave the way towards building a multi-stage broadband topologically protected delay line capable of buffering multiple acoustic pulses.

Beyond valley-Hall phases within a single SC, layer-mixed and layer-polarized topological valley Hall phases were recently proposed by Lu et al.<sup>81</sup>, using a unique design of bilayer sonic crystals (BSCs). Figure 5a illustrates the schematic of the unit cell of the BSC, which is composed of two layers of finite SCs sandwiched between a pair of rigid plates and separated by a plate that is pierced with a honeycomb array of circular holes. Each layer consists of a hexagonal array of regular triangular rods. As a result, the degree of freedoms of orientations is broad with respect to the relative angle  $\alpha$  and the common angle  $\beta$ . Figure 5b depicts a phase diagram in the entire angular domain, illustrating straight and curved lines, which are associated with ring and point degeneracies, respectively. The shaded regions represent the nontrivial AVH phases that are characterized by the quantized topological invariant  $C_V^K$  associated to the single-layer system, whereas the remaining regions of the phase diagram represent nontrivial acoustic layer-valley Hall (ALH) phases, characterized by  $C_L^K$ . To observe the differences between those phase, dispersion relations of ribbon-shaped BSCs are studied: first, a BSCs

composed with rod orientations  $(0, \pm 20^\circ)$ , which belong to different AVH phases ( $\Delta C_V^K = 2$ ). As shown in Fig. 5c, two edge modes with positive group velocities appear at the K valley (red curves) and two other edge modes with opposite group velocities (blue curves) appear at the  $K'$  valley due to the time-reversal symmetry. The eigenfields are located in both layers (see insets). Second, a BSCs is composed with rod orientations  $(\pm 10^\circ, 3^\circ)$ , which belong to different ALH phases ( $\Delta C_L^K = 2$ ). Compared to the AVH scenario, the group velocities of the two edge modes at the K valley are opposite. The eigenfield concentrates predominantly in either the upper layer or the lower one (Fig. 5d). That is to say, for the edge state projected by the same valley, sound waves propagate towards one side in the upper layer and towards another side in the lower layer without any interference with each other, which is equivalent to spin-orbital couplings in electronic systems. As shown in Fig. 5e, an efficient inter-layer converter can be constructed by four distinct BSC phases that support ALH (bilateral) and AVH (middle) edge modes along the interfaces in the x-direction. Most of the sound energy radiated from a point source located at the left side of the upper layers can be transferred to the lower layer as the wave reaches another ALH interface.

### Three dimensional topological acoustics

Parallel to developments of TIs, topological semimetals have emerged as a new frontier in the quest of new topological phases in the past few years<sup>16,17</sup>. Topological semimetals are identified as topological materials in the sense that the gapless band structures are topologically protected and are accompanied by robust gapless surface states<sup>18</sup>. Weyl semimetal, as an important member of the topological semimetals, has received quite a bit of attention

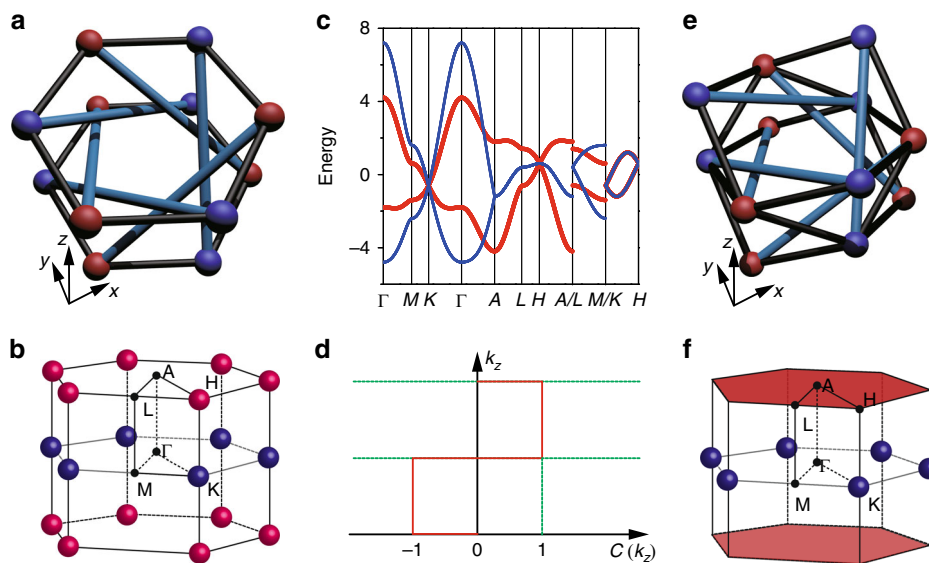


**Fig. 6** Weyl semimetal and topological charged nodal surface semimetal. **a, e** Show the tight-binding model of a system possessing Weyl points and a charged nodal surface, respectively. **b, f** Show the topological charge distribution in the reciprocal space for the tight-binding model in **a, e**, respectively, where the red and blue spheres represent Weyl points with charge +1 and -1, respectively, and the red surface represents a nodal surface with topological charge +2. Some high symmetry points in the first Brillouin zone are also labeled. **c** shows the band structure, where  $t_0 = 1$  and  $t_c = 0.2$  are used. Here red and blue correspond to the tight-binding model in **a, e**, respectively. **d** shows the Chern number as a function of  $k_z$ , which changes at  $k_z = 0$  and  $k_z = \pi$

recently with the theoretical discovery and experimental realizations in electronic and photonic systems<sup>82–86</sup>. Soon after that, acoustic Weyl metacrystals were discovered in coupled resonators and waveguides<sup>87,88</sup> and experimentally demonstrated very recently<sup>89–91</sup>. In addition to airborne sound waves<sup>87–91</sup>, Weyl points have also been investigated in elastic waves<sup>92,93</sup>. To illustrate the physics, we focus on airborne sound waves.

Weyl semimetals are periodic systems that possess Weyl points<sup>94</sup>, which are topological robust band degeneracy points. The Hamiltonian which describes a Weyl point with a topological charge of +1 or -1 is given by

$$\hat{H}(q) = f(q)\sigma_0 + \sum_{i,j=x,y,z} q_i v_{i,j} \sigma_j, \quad (5)$$

where  $q = (q_x, q_y, q_z)$  and  $q_i$  is the wave vector originating from the Weyl point,  $f(q)$  is an arbitrary real function of  $q$ ,  $v$  is a  $3 \times 3$  constant matrix,  $\sigma_0$  is the  $2 \times 2$  unit matrix, and  $\sigma_x, \sigma_y, \sigma_z$  are the Pauli matrices. The charge of the Weyl point in Eq. (5) is given by  $C = \text{sgn}(\det v)$ . Weyl points can also exhibit higher topological charges<sup>95</sup>. For simplicity sake, we restrict our discussion here to Weyl points of charge +1 and -1. Weyl points are robust against any perturbations which keep the wave vectors as good quantum numbers. This can also be seen from the fact that the Weyl Hamiltonian contains all the Pauli matrices and hence local perturbation can only serve to shift the Weyl point in momentum space but cannot open a band gap. A Weyl point can only be “annihilated” by another Weyl point which carries the opposite topological charge and a band gap can be opened if Weyl points carrying opposite charges collide in momentum space.

Acoustic Weyl metacrystals were discussed in 2015 in a system composing of coupled resonators and coupled waveguides<sup>87</sup>. Fig. 6a shows the schematic picture of a tight-binding model that explains the formation Weyl points in the reciprocal space for that particular system. This tight-binding model can be regarded as an AA stacking of graphene lattice along the  $z$ -direction, where the red and blue spheres represent different sublattices and the black bonds represent intralayer hopping with hopping strength  $t_0$ . Interlayer hopping is represented by the cyan bonds and with hopping strength  $t_c$ . In this tight-binding model, time-reversal

symmetry is preserved and hence both  $t_0$  and  $t_c$  are real constants. The Hamiltonian  $\hat{H}$  of this tight-binding model is given by:

$$\hat{H} = \sum_{\langle i,j \rangle} t_0 b_{i,k}^\dagger a_{j,k} + \sum_{\langle\langle i,j \rangle\rangle} t_c (a_{i,k+1}^\dagger a_{j,k} + b_{i,k+1}^\dagger b_{j,k}) + H.c., \quad (6)$$

where  $a(b)$  and  $a^\dagger(b^\dagger)$  are the annihilation and creation operators on the sublattice sites. Each lattice site is labeled by  $i, k$ , wherein the first denotes the coordinate inside each layer and the second denotes the layer number.  $\langle i, j \rangle$  in the first summation represents intralayer nearest neighbor and  $\langle\langle i, j \rangle\rangle$  in the second summation represents interlayer next nearest neighbor. The corresponding Bloch Hamiltonian  $H(k)$  is given by

$$\hat{H}(k) = (t_c g(k_z) t_0 h(k_x, k_y) t_0 [h(k_x, k_y)]^* t_c g(-k_z)) \quad (7)$$

where

$g(k) = 2\cos(k_x a + k_z d_h) + 4\cos(\sqrt{3}k_y a/2)\cos(k_x a/2 - k_z d_h)$  and  $h(k_x, k_y) = \exp(-i\sqrt{3}k_y a/3) + 2\cos(k_x a/2)\exp(i\sqrt{3}k_y a/6)$  with  $a$  and  $d_h$  being the lattice constants of the graphene lattice and along the  $z$ -direction, respectively.

The first Brillouin zone of this tight-binding model is shown in Fig. 6b with some high symmetry points also being labeled. The band structures along some high symmetric directions are shown in Fig. 6c with the red curve, where the hopping parameters are taken to be  $t_0 = 1$  and  $t_c = 0.2$ . The band dispersions are linear near the points  $K$  and  $H$  along all the high symmetric directions, which indicates that this tight-binding model possesses Weyl points at  $K$  and  $H$  as well as  $K'$  and  $H'$ . To see this point, we expand the Hamiltonian in Eq. (6) around  $K = (0, 4\pi a/3, 0)$ . Keeping only to the lowest order, we get

$$\hat{H}(q) = -3t_c \sigma_0 + 3\sqrt{3}t_c q_z \sigma_z - \frac{\sqrt{3}}{2} t_0 (q_y \sigma_y - q_x \sigma_x). \quad (8)$$

The first term in Eq. (8) represents an energy shift which does not change the topological charge of the Weyl point. And hence the charge of the Weyl point at  $K$  is -1. The system exhibits  $C_6$  rotational symmetry along the  $z$ -direction, and time-reversal

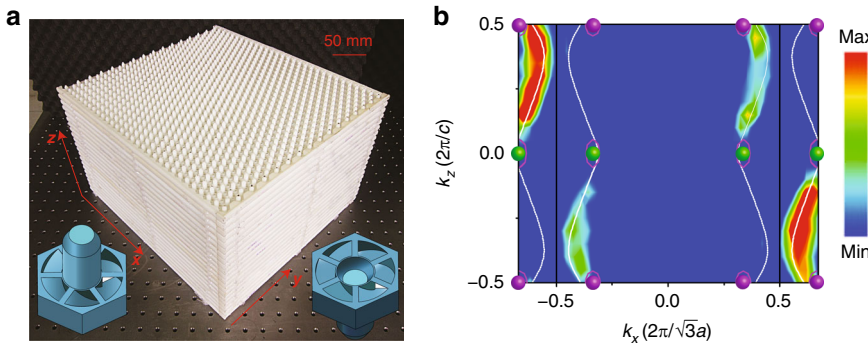


**Fig. 7** Experimental observation of acoustic Fermi-arcs in ref. <sup>89</sup>. **a** A photo of the sample, where the insets show the front (lower left) and back (lower right) views of the unit cell. **b** Fermi-arcs measured using Fourier transforms of surface wave fields

symmetry implies that the system possesses another Weyl point at the  $K'$  point and with the same charge. One can also follow the same procedure and concludes that the charge of the Weyl point at  $H$  is +1. This fact also illustrates an important property of Weyl crystals: the total charge inside the first Brillouin zone of a periodic system should vanish. This distribution of the Weyl points and their associated topological charges are shown in Fig. 6b.

In this system,  $k_z$  is a good quantum number, and hence one can define the Chern number of any two-dimensional subsystems with a fixed  $k_z$ . In Fig. 6d, we show the Chern number as a function of  $k_z$  with the red curve. The Chern number only changes when it comes across a  $k_z$  plane with nonzero topological charge. In this system, the Chern number is +1 for  $k_z > 0$  and -1 for  $k_z < 0$ . According to the bulk-edge correspondence, there should be one-way edge states provided that  $k_z$  is preserved. Such one-way edge states should be present for any  $k_z \neq 0$  or  $\pi$  which then forms a Riemann surface like structure and the iso-energy contour of it is known as the Fermi arc<sup>17</sup>.

Weyl points are not the only object in the reciprocal space that possesses a topological charges<sup>96</sup>. A nodal surface, which is a surface degeneracy between two bands, can also possess a non-zero topological charge. The nodal surface is protected by non-symmorphic symmetry  $G_{2z} \equiv \mathcal{T}\tilde{C}_{2z}$  and is located at  $k_z = \pi/d_h$  with arbitrary  $k_x$  and  $k_y$ , where  $\mathcal{T}$  denotes the time-reversal operation and  $\tilde{C}_{2z}$  represents the two-fold screw rotational symmetry along the  $z$ -direction. The band dispersion is linear in the vicinity of the nodal surface. Note here that  $G_{2z}$  symmetry only protects the presence of the nodal surface, whether it is topologically charged or not depends on the system parameters<sup>96</sup>. A tight-binding model that exhibits this symmetry and also possesses a charged nodal surface can be obtained by simply shifting one of the sublattice in Fig. 6a along the  $z$ -direction by  $d_h/2$ , and the resulting tight-binding model is shown in Fig. 6e. Here, the intralayer hopping is also slightly modified to preserve the  $G_{2z}$  symmetry. The band structure of this tight-binding model is shown in Fig. 6c with the blue curve. Here the intralayer hopping (denoted by the black bonds) and interlayer hopping (denoted by the cyan bonds) are set as  $t_0 = 1$  and  $t_c = 0.2$ , respectively. We see that the two bands become degenerate on the  $k_z = \pi$  plane and the dispersion is linear away from this nodal surface. The Weyl points at  $K$  and  $K'$  still are preserved while the Weyl points at  $H$  and  $H'$  are merged into the nodal surface and hence the nodal surface should possess topological charge +2. The charge distribution of the tight-binding model in Fig. 6e is shown in Fig. 6f, where the red plane represents the nodal surface with topological charge +2. The Chern numbers as a function of  $k_z$  remain the same as that in Fig. 6d.

One advantage of using acoustic metamaterial as a platform to explore the physics of topological material is that real samples can

be made more straightforwardly than quantum materials. Indeed, experimental realizations of acoustic Weyl metacrystals were performed soon after the theoretical proposal<sup>89,90</sup>. We focus on the experiments in ref. <sup>89</sup>. In this work, the authors realized an acoustic Weyl metacrystal, measured the Fermi arc and demonstrated the robustness of the surface states. Figure 7a shows the experimental sample and the insets show the front (lower left) and back (lower right) views of the unit cell. The sample was fabricated by 3D printing technology, and the printed structure can be treated as sound hard where the sound waves cannot penetrate. The detail geometric parameters can be found in ref. <sup>89</sup>. In this system, the Weyl points with opposite charges are not related by any symmetry and hence their frequencies can be different. The frequencies of the Weyl points under consideration at  $K$  and  $H$  are 15 kHz and 16 kHz, respectively. Figure 7b shows the surface Brillouin zone on the  $k_x-k_z$  plane and projection of Weyl points as denoted by the green and purple spheres. The solid and dashed curves represent the “Fermi arcs” on the positive and negative  $x-z$  surfaces, respectively. The working frequency is chosen to be 15.4 kHz which is between the frequencies of these two Weyl points. At this frequency, the equi-frequency contours of the bulk bands around the Weyl points project to elliptical disks as outlined by the purple curves. The Fermi arcs connect these elliptical disks. Experimentally, one can measure the surface wave field distributions which can be Fourier transformed to obtain the Fermi arc. The experimental results are shown as color code in Fig. 7b, where red represents maximal value and blue represents minimal value. The experimentally measured results agree quite well with the numerical simulations. As discussed before, such systems support one-way surface states against  $k_z$  preserved scatterings, which are also experimentally demonstrated<sup>89,90</sup>.

### Topological mechanical waves

In the preceding sections, we reviewed the entire landscape of topological states in both time-reversal symmetric and asymmetric acoustic structures. It is thus evident that these quantum topological phenomena, similar to photonic systems, find their counterparts in engineered sonic structures and lattices. But does this apply to mechanical waves as well? Throughout this review, we have hinted towards it, first of all however, we need to distinguish between zero frequency nontrivial topological modes that are insensitive to smooth deformations and actual mechanical vibrations. In this section, we embark to discuss on the latter whereas topological zero modes and states of self-stress have been extensively discussed elsewhere<sup>97</sup>. The study into topologically protected mechanical waves at finite frequencies has been largely triggered by the search of related phenomena for other areas of classical physics<sup>98,99</sup>. Hence, for elastic vibrations and mechanical waves, equivalent to the preceding sections we discriminate

between systems of intact and broken time-reversal symmetry, which will ultimately give rise interface-supporting modes in the form of helical spin-polarized and chiral one-way edge states, respectively. Gyroscopic lattices are prominent candidates capable to form forbidden regions, band gaps, in which bulk vibrations are inhibited. The opening of such gap is induced by breaking the  $T$  symmetry through rotating gyroscopes permitting waves to sustain only in the form of unidirectional and topological robust chiral edge states along finite sample interfaces<sup>100,101</sup>.

In order to mimic with mechanical waves the QSHE and launching helical edge vibrations at interfaces one can revert to passive systems, i.e.,  $T$  symmetric structures in no need for an external bias to violate reciprocity. In order to keep the  $T$  symmetry intact, two opposite counter-propagating spins have to coexist at the same frequency according to Kramers degeneracy theorem. Hence, helical edge states have been detected in pendula lattices<sup>102,103</sup> and predicted for Lamb and flexural waves in structured plates<sup>104,105</sup> and granular crystals<sup>106</sup>.

As detailed above, in addition to the pseudo spin, sound waves are capable of emulating a valley degree of freedom. Rather than pursuing novel carriers of information and energy similar to their electronic counterpart, recent efforts in the literature have demonstrated that valley Hall polarized mechanical states can give rise to topological protected vibrations. In order to gap the Dirac cones of phononic lattices, the inversion symmetries were broken by introducing a hexagonal boron nitride-like geometry of unequal masses within the unit cell. It was shown that these elastic systems contain topologically nontrivial band gaps hosting backscattering suppressed edge states<sup>107,108</sup>. Similar efforts have been devoted to observe topologically valley-polarized states in bilayers, slender veins connected rod-crystals, thin plates, and diatomic waveguides<sup>75,109–111</sup>.

Recently, on the nanoscale, chiral phonons were observed in monolayer tungsten diselenide whose broken  $P$  symmetry splits clockwise and counterclockwise motions into nondegenerate states, which has great potential for the realization of phonon-driven topological states and controlled intervalley scattering<sup>112</sup>. These topological states are based on atomic-scale lattice vibrations that differ substantially from the previously mentioned states in macroscopical artificial crystals with lattice constants in the  $mm$  to  $cm$  range. Along the same frontier, Weyl phonons have been predicted in magnetic- and transition metals. In the latter case, double Weyl points are hosted throughout the phonon spectrum thanks to the noncentrosymmetric but  $T$  symmetric crystalline structure<sup>113</sup>. In contrast, in the former case, it was shown that strong circular phonon dichroism can be induced in Weyl semimetals with both of broken  $P$  and  $T$  symmetry<sup>114</sup>. These findings have the possibility to open doors for topological phononics at the atomic scale comprising engineering surface phonons and heat transport related to the phonon Hall effect<sup>115</sup>.

Other exciting explorations along the mechanical research frontier of topological insulators show how smooth deformations can provide topological phase transitions, pseudomagnetism for sound is created, and how mechanical quadrupole topological insulators sustain corner states<sup>78,116,117</sup>. Conclusively, these tremendous efforts demonstrate that man-made artificial crystals serve as a fruitful playground to test with mechanical vibrations topologically protected wave propagation.

## Future directions

We have reviewed recent efforts in putting topological acoustics on the map of an overall attempt in building the bridge between quantum physics and topological insulators for classical waves. Artificial macroscopic lattices in the form of sonic and phononic crystals pose only little fabrication challenges as compared to photonic systems that are built on much smaller scales at which imperfections matter. Concerning this, it did not take much time for the frontier of topological acoustics to flourish from 2D to 3D

where theoretical predictions quickly turned into experimental proofs of concepts.

The strategy to move forward could potentially rest on looking into the current state-of-the-art comprising electronic and photonic topological systems. Doing this will certainly provide a platform for research into exotic sound propagation and mechanical vibrations to spearhead novel basic wave physics. Topics such as higher-order topological insulators (HOTI)<sup>117</sup> sustaining corner and hinge states, experimental progress in non-Hermitian and  $PT$  symmetry topological insulators<sup>118</sup>, and analogies of Majorana-like bound states at finite frequencies will fall into this category making topological acoustics relevant among condensed-matter physicists. However, it is of substantial significance to actually look at the specific targets of research in acoustics and elasticity together with their more technological oriented challenges. Realizing topological robust and defect insensitive wave guiding, signal buffering and splitting could provide new avenues for improved surface acoustic waves sensors, on-chip filters in mobile phones, enhanced coupling efficiency in touchscreens, and potentially improve the robustness of bio-chemical sensing. Along this line, efforts in the near future must therefore revolve around shrinking topological acoustical but also mechanical properties into the micro scale in order to be of relevance to the aforementioned technologies.

Conclusively, while many of the reviewed results and breakthrough findings, for the most part, can be categorized in terms of academic research, based on the unconventional way sound and vibrations are tailored, one can only look forward to unprecedented routes and possibilities for phononic technologies that fully take advantage of topologically robust wave control.

## Data availability

The related data are available from the corresponding authors on request.

Received: 25 June 2018 Accepted: 19 November 2018

Published online: 21 December 2018

## References

- Read, N. Topological phases and quasiparticle braiding. *Phys. Today* **65**, 38 (2012).
- Klitzing, Kv, Dorda, G. & Pepper, M. New method for high-accuracy determination of the fine-structure constant based on quantized hall resistance. *Phys. Rev. Lett.* **45**, 494 (1980). *The paper discovering the quantum Hall effect, the first observation of the topological phases of matter.*
- Laughlin, R. B. Quantized hall conductivity in two dimensions. *Phys. Rev. B* **23**, 5632 (1981). *The paper toward explaining von Klitzings discovery on the unexpected precision of the integral Hall conductance plateaus.*
- Thouless, D. J., Kohmoto, M., Nightingale, M. P. & Den Nijs, M. Quantized hall conductance in a two-dimensional periodic potential. *Phys. Rev. Lett.* **49**, 405 (1982). *The recognition of the fact that the quantized Hall conductance (at the plateaus) for quantum Hall effect has topological significance.*
- Berry, M. V. Quantal phase factors accompanying adiabatic changes. *Proc. R. Soc. Lond. A Math. Phys. Sci.* **392**, 45–57 (1984).
- Haldane, F. D. M. Model for a quantum hall effect without landau levels: condensed-matter realization of the “parity anomaly”. *Phys. Rev. Lett.* **61**, 2015 (1988).
- Kane, C. L. & Mele, E. J. Quantum spin hall effect in graphene. *Phys. Rev. Lett.* **95**, 226801 (2005).
- Fu, L., Kane, C. L. & Mele, E. J. Topological insulators in three dimensions. *Phys. Rev. Lett.* **98**, 106803 (2007).
- Bernevig, B. A., Hughes, T. L. & Zhang, S.-C. Quantum spin hall effect and topological phase transition in HgTe quantum wells. *Science* **314**, 1757 (2006). *The experimental observation of the quantum spin Hall effect, paving the way toward electrical manipulation of spins and spin currents with little or no dissipation.*
- König, M. et al. Quantum spin hall insulator state in HgTe quantum wells. *Science* **318**, 766 (2007).
- Hasan, M. Z. & Kane, C. L. Colloquium: topological insulators. *Rev. Mod. Phys.* **82**, 3045 (2010).

12. Qi, X.-L. & Zhang, S.-C. Topological insulators and superconductors. *Rev. Mod. Phys.* **83**, 1057 (2011).
13. Sheng, L., Sheng, D., Ting, C. & Haldane, F. Nondissipative spin hall effect via quantized edge transport. *Phys. Rev. Lett.* **95**, 136602 (2005).
14. Yao, W., Xiao, D. & Niu, Q. Valley-dependent optoelectronics from inversion symmetry breaking. *Phys. Rev. B* **77**, 235406 (2008).
15. Ju, L. et al. Topological valley transport at bilayer graphene domain walls. *Nature* **520**, 650 (2015).
16. Burkov, A. A. Topological semimetals. *Nat. Mater.* **15**, 1145–1148 (2016).
17. Fang, C., Weng, H., Dai, X. & Fang, Z. Topological nodal line semimetals. *Chin. Phys. B* **25**, 117106 (2016).
18. Burkov, A. A., Hook, M. D. & Balents, L. Topological nodal semimetals. *Phys. Rev. B* **84**, 235126 (2011).
19. Haldane, F. & Raghu, S. Possible realization of directional optical waveguides in photonic crystals with broken time-reversal symmetry. *Phys. Rev. Lett.* **100**, 013904 (2008). *The realisation of analogue quantum Hall effect in photonic system, therefore opening new chapter for topological phases in classical regime.*
20. Wang, Z., Chong, Y., Joannopoulos, J. D. & Soljačić, M. Observation of unidirectional backscattering-immune topological electromagnetic states. *Nature* **461**, 772 (2009).
21. Fleury, R., Sounas, D. L., Sieck, C. F., Haberman, M. R. & Alù, A. Sound isolation and giant linear nonreciprocity in a compact acoustic circulator. *Science* **343**, 516–519 (2014).
22. Ni, X. et al. Topologically protected one-way edge mode in networks of acoustic resonators with circulating air flow. *New J. Phys.* **17**, 053016 (2015).
23. Yang, Z. et al. Topological acoustics. *Phys. Rev. Lett.* **114**, 114301 (2015).
24. Khanikaev, A. B., Fleury, R., Mousavi, S. H. & Alù, A. Topologically robust sound propagation in an angular-momentum-biased graphene-like resonator lattice. *Nat. Commun.* **6**, 8260 (2015).
25. Chen, Z.-G. & Wu, Y. Tunable topological phononic crystals. *Phys. Rev. Appl.* **5**, 054021 (2016).
26. Chen, Z.-G., Zhao, J., Mei, J. & Wu, Y. Acoustic frequency filter based on anisotropic topological phononic crystals. *Sci. Rep.* **7**, 15005 (2017).
27. Zhang, X. & Liu, Z. Extremal transmission and beating effect of acoustic waves in two-dimensional sonic crystals. *Phys. Rev. Lett.* **101**, 264303 (2008).
28. Torrent, D. & Sánchez-Dehesa, J. Acoustic analogue of graphene: observation of dirac cones in acoustic surface waves. *Phys. Rev. Lett.* **108**, 174301 (2012).
29. Torrent, D., Mayou, D. & Sánchez-Dehesa, J. Elastic analog of graphene: Dirac cones and edge states for flexural waves in thin plates. *Phys. Rev. B* **87**, 115143 (2013).
30. Zhu, Y. et al. Experimental realization of acoustic chern insulator. Preprint at <https://arxiv.org/abs/1801.07942> (2018).
31. Souslov, A., van Zuiden, B. C., Bartolo, D. & Vitelli, V. Topological sound in active-liquid metamaterials. *Nat. Phys.* **13**, 1091 (2017).
32. Shankar, S., Bowick, M. J. & Marchetti, M. C. Topological sound and flocking on curved surfaces. *Phys. Rev. X* **7**, 031039 (2017).
33. Sheng, D., Weng, Z., Sheng, L. & Haldane, F. Quantum spin-Hall effect and topologically invariant Chern numbers. *Phys. Rev. Lett.* **97**, 036808 (2006).
34. He, C. et al. Photonic topological insulator with broken time-reversal symmetry. *Proc. Natl Acad. Sci. USA* **113**, 4924–4928 (2016).
35. Khanikaev, A. B. et al. Photonic topological insulators. *Nat. Mater.* **12**, 233 (2013).
36. Ma, T., Khanikaev, A. B., Mousavi, S. H. & Shvets, G. Guiding electromagnetic waves around sharp corners: topologically protected photonic transport in metawaveguides. *Phys. Rev. Lett.* **114**, 127401 (2015).
37. Peng, Y.-G. et al. Experimental demonstration of anomalous floquet topological insulator for sound. *Nat. Commun.* **7**, 13368 (2016).
38. He, C. et al. Topological phononic states of underwater sound based on coupled ring resonators. *Appl. Phys. Lett.* **108**, 031904 (2016).
39. Wu, L.-H. & Hu, X. Scheme for achieving a topological photonic crystal by using dielectric material. *Phys. Rev. Lett.* **114**, 223901 (2015).
40. Zhang, Z. et al. Topological creation of acoustic pseudospin multipoles in a flow-free symmetry-broken metamaterial lattice. *Phys. Rev. Lett.* **118**, 084303 (2017).
41. Deng, Y., Ge, H., Tian, Y., Lu, M. & Jing, Y. Observation of zone folding induced acoustic topological insulators and the role of spin-mixing defects. *Phys. Rev. B* **96**, 184305 (2017).
42. Chen, Z.-G. et al. Accidental degeneracy of double dirac cones in a phononic crystal. *Sci. Rep.* **4**, 4613 (2014).
43. He, C. et al. Acoustic topological insulator and robust one-way sound transport. *Nat. Phys.* **12**, 1124 (2016). *The experimental realisation of analogue quantum spin Hall effect in acoustics via the construction of pseudospins to mimic spin polarizations in electronic systems.*
44. Mei, J., Chen, Z. & Wu, Y. Pseudo-time-reversal symmetry and topological edge states in two-dimensional acoustic crystals. *Sci. Rep.* **6**, 32752 (2016).
45. Yu, S. et al. A monolithic topologically protected phononic circuit. Preprint at <https://arxiv.org/abs/1707.04901> (2017).
46. Rycerz, A., Tworzydlo, J. & Beenakker, C. W. J. Valley filter and valley valve in graphene. *Nat. Phys.* **3**, 172–175 (2007).
47. Xiao, D., Yao, W. & Niu, Q. Valley-contrasting physics in graphene: magnetic moment and topological transport. *Phys. Rev. Lett.* **99**, 236809 (2007).
48. Semenoff, G. W., Semenoff, V. & Zhou, F. Domain walls in gapped graphene. *Phys. Rev. Lett.* **101**, 087204 (2008).
49. Martin, I., Blanter, Y. M. & Morpurgo, A. F. Topological confinement in bilayer graphene. *Phys. Rev. Lett.* **100**, 036804 (2008).
50. Zhang, F., Jung, J., Fiete, G. A., Niu, Q. & MacDonald, A. H. Spontaneous quantum hall states in chirally stacked few-layer graphene systems. *Phys. Rev. Lett.* **106**, 156801 (2011).
51. Zhang, X. Observing zitterbewegung for photons near the dirac point of a two-dimensional photonic crystal. *Phys. Rev. Lett.* **100**, 113903 (2008).
52. Sepkhanov, R. A., Nilsson, J. & Beenakker, C. W. J. Proposed method for detection of the pseudospin-1/2 berry phase in a photonic crystal with a dirac spectrum. *Phys. Rev. B* **78**, 045122 (2008).
53. Zandbergen, S. R. & de Dood, M. J. A. Experimental observation of strong edge effects on the pseudodiffusive transport of light in photonic graphene. *Phys. Rev. Lett.* **104**, 043903 (2010).
54. Bittner, S. et al. Observation of a dirac point in microwave experiments with a photonic crystal modeling graphene. *Phys. Rev. B* **82**, 014301 (2010).
55. Weick, G., Woollattoc, C., Barnes, W. L., Hess, O. & Mariani, E. Dirac-like plasmons in honeycomb lattices of metallic nanoparticles. *Phys. Rev. Lett.* **110**, 106801 (2013).
56. Dong, J.-W., Chen, X.-D., Zhu, H., Wang, Y. & Zhang, X. Valley photonic crystals for control of spin and topology. *Nat. Mater.* **16**, 298 (2017).
57. Chen, X.-D., Zhao, F.-L., Chen, M. & Dong, J.-W. Valley-contrasting physics in all-dielectric photonic crystals: orbital angular momentum and topological propagation. *Phys. Rev. B* **96**, 020202 (2017).
58. Yang, Y., Jiang, H. & Hang, Z. H. Topological valley transport in two-dimensional honeycomb photonic crystals. *Sci. Rep.* **8**, 1588 (2018).
59. Hafezi, M., Demler, E. A., Lukin, M. D. & Taylor, J. M. Robust optical delay lines with topological protection. *Nat. Phys.* **7**, 907 (2011).
60. Ma, T. & Shvets, G. All-Si valley-Hall photonic topological insulator. *New J. Phys.* **18**, 025012 (2016).
61. Gao, F. et al. Topologically protected refraction of robust kink states in valley photonic crystals. *Nat. Phys.* **14**, 140 (2018).
62. Lai, K., Ma, T., Bo, X., Anlage, S. & Shvets, G. Experimental realization of a reflections-free compact delay line based on a photonic topological insulator. *Sci. Rep.* **6**, 28453 (2016).
63. Wu, X. et al. Direct observation of valley-polarized topological edge states in designer surface plasmon crystals. *Nat. Commun.* **8**, 1304 (2017).
64. Noh, J., Huang, S., Chen, K. P. & Rechtsman, M. C. Observation of photonic topological valley hall edge states. *Phys. Rev. Lett.* **120**, 063902 (2018).
65. Gao, Z. et al. Valley surface-wave photonic crystal and its bulk/edge transport. *Phys. Rev. B* **96**, 201402 (2017).
66. Zhang, F. Brought to light. *Nat. Phys.* **14**, 111–113 (2018).
67. Ye, L., Yang, Y., Hang, Z. H., Qiu, C. & Liu, Z. Observation of valley-selective microwave transport in photonic crystals. *Appl. Phys. Lett.* **111**, 251107 (2017).
68. Lu, J. et al. Dirac cones in two-dimensional artificial crystals for classical waves. *Phys. Rev. B* **89**, 134302 (2014).
69. Lu, J., Qiu, C., Ke, M. & Liu, Z. Valley vortex states in sonic crystals. *Phys. Rev. Lett.* **116**, 093901 (2016).
70. Ye, L. et al. Observation of acoustic valley vortex states and valley-chirality locked beam splitting. *Phys. Rev. B* **95**, 174106 (2017).
71. Lu, J. et al. Observation of topological valley transport of sound in sonic crystals. *Nat. Phys.* **13**, 369–374 (2017). *Experimental demonstration of topological valley transport in acoustics.*
72. Xia, B.-Z. et al. Observation of valleylike edge states of sound at a momentum away from the high-symmetry points. *Phys. Rev. B* **97**, 155124 (2018).
73. Zhang, Z. et al. Topological acoustic delay line. *Phys. Rev. Appl.* **9**, 034032 (2018).
74. Wen, X. et al. Acoustic Dirac degeneracy and topological phase transitions realized by rotating scatterers. *J. Appl. Phys.* **123**, 091703 (2018).
75. Huo, S.-Y., Chen, J.-I., Huang, H.-B. & Huang, G.-L. Simultaneous multiband valley protected topological edge states of shear vertical wave in two dimensional phononic crystals with veins. *Sci. Rep.* **7**, 10335 (2017).
76. Yang, Y., Yang, Z. & Zhang, B. Acoustic valley edge states in a graphene-like resonator system. *J. Appl. Phys.* **123**, 091713 (2018).
77. Zhang, Z. et al. Directional Acoustic Antennas Based on Valley-Hall Topological Insulators. *Adv. Mater.* **30**, 1803229 (2018).
78. Brendel, C., Peano, V., Painter, O. J. & Marquardt, F. Pseudomagnetic fields for sound at the nanoscale. *Proc. Natl Acad. Sci. USA* **114**, E3390–E3395 (2017).
79. Ezawa, M. Topological kirchhoff law and bulk-edge correspondence for valley chern and spin-valley chern numbers. *Phys. Rev. B* **88**, 161406 (2013).
80. Mong, R. S. K. & Shivamoggi, V. Edge states and the bulk-boundary correspondence in dirac hamiltonians. *Phys. Rev. B* **83**, 125109 (2011).

81. Lu, J. et al. Valley topological phases in bilayer sonic crystals. *Phys. Rev. Lett.* **120**, 116802 (2018).
82. Fang, Z. et al. The anomalous hall effect and magnetic monopoles in momentum space. *Science* **302**, 92–95 (2003).
83. Burkov, A. A. & Balents, L. Weyl semimetal in a topological insulator multilayer. *Phys. Rev. Lett.* **107**, 127205 (2011).
84. Wan, X., Turner, A. M., Vishwanath, A. & Savrasov, S. Y. Topological semimetal and fermi-arc surface states in the electronic structure of pyrochlore iridates. *Phys. Rev. B* **83**, 205101 (2011).
85. Lu, L., Fu, L., Joannopoulos, J. D. & Soljačić, M. Weyl points and line nodes in gyroid photonic crystals. *Nat. Photon.* **7**, 294–299 (2013).
86. Lu, L., Fu, L., Joannopoulos, J. D. & Soljačić, M. Experimental observation of weyl points. *Science* **349**, 622–624 (2015).
87. Xiao, M., Chen, W.-J., He, W.-Y. & Chan, C. T. Synthetic gauge flux and weyl points in acoustic systems. *Nat. Phys.* **11**, 920–924 (2015). *Theoretical realization of an acoustic Weyl metacrystal composing of coupled resonators and waveguides*.
88. Yang, Z. & Zhang, B. Acoustic type-ii weyl nodes from stacking dimerized chains. *Phys. Rev. Lett.* **117**, 224301 (2016).
89. Li, F., Huang, X., Lu, J., Ma, J. & Liu, Z. Weyl points and fermi arcs in a chiral phononic crystal. *Nat. Phys.* **14**, 30–34 (2018). *Experimental demonstration of an acoustic Weyl metacrystal*.
90. Ge, H. et al. Experimental observation of acoustic weyl points and topological surface states. Preprint at <https://arxiv.org/abs/1803.00828> (2018).
91. He, H. et al. Topological negative refraction of surface acoustic waves in a Weyl phononic crystal. *Nature* **560**, 61 (2018). *Experimental demonstration of topological negative refraction*.
92. Wang, Y.-T. Multiple weyl and double-weyl points in an elastic chiral lattice. Preprint at <https://arxiv.org/abs/1803.03183> (2018).
93. Fruchart, M. et al. Soft self-assembly of weyl materials for light and sound. *Proc. Natl Acad. Sci. USA* **115**, E3655–E3664 (2018).
94. Weyl, H. Elektron und gravitation. i. *Z. für Phys.* **56**, 330–352 (1929).
95. Fang, C., Gilbert, M. J., Dai, X. & Bernevig, B. A. Multi-weyl topological semimetals stabilized by point group symmetry. *Phys. Rev. Lett.* **108**, 266802 (2012).
96. Xiao, M. & Fan, S. Topologically charged nodal surface. Preprint at <https://arxiv.org/abs/1709.02363> (2017).
97. Bertoldi, K., Vitelli, V., Christensen, J. & van Hecke, Martin Flexible mechanical metamaterials. *Nat. Rev. Mater.* **2**, 17066 (2017).
98. Peano, V., Brendel, C., Schmidt, M. & Marquardt, F. Topological phases of sound and light. *Phys. Rev. X* **5**, 031011 (2015).
99. Liu, Y., Xu, Y., Zhang, S.-C. & Duan, W. Model for topological phononics and phonon diode. *Phys. Rev. B* **96**, 064106 (2017).
100. Wang, P., Lu, L. & Bertoldi, K. Topological phononic crystals with one-way elastic edge waves. *Phys. Rev. Lett.* **115**, 104302 (2015).
101. Nash, L. M. et al. Topological mechanics of gyroscopic metamaterials. *Proc. Natl Acad. Sci. USA* **112**, 14495–14500 (2015).
102. Süsstrunk, R. & Huber, S. D. Observation of phononic helical edge states in a mechanical topological insulator. *Science* **349**, 47–50 (2015).
103. Salerno, G. et al. Spin orbit coupling in a hexagonal ring of pendula. *New J. Phys.* **19**, 055001 (2017).
104. Mousavi, S. H., Khanikaev, A. B. & Wang, Z. Topologically protected elastic waves in phononic metamaterials. *Nat. Commun.* **6**, 8682 (2015).
105. Chaunsali, R., Chen, C.-W. & Yang, J. Subwavelength and directional control of flexural waves in zone-folding induced topological plates. *Phys. Rev. B* **97**, 054307 (2018).
106. Zheng, L.-Y., Theocharis, G., Tournat, V. & Gusev, V. Quasitopological rotational waves in mechanical granular graphene. *Phys. Rev. B* **97**, 060101 (2018).
107. Pal, R. K. & Ruzzene, M. Edge waves in plates with resonators: an elastic analogue of the quantum valley hall effect. *New J. Phys.* **19**, 025001 (2017).
108. Vila, J., Pal, R. K. & Ruzzene, M. Observation of topological valley modes in an elastic hexagonal lattice. *Phys. Rev. B* **96**, 134307 (2017).
109. Pal, R. K., Schaeffer, M. & Ruzzene, M. Helical edge states and topological phase transitions in phononic systems using bilayered lattices. *J. Appl. Phys.* **119**, 084305 (2016).
110. Wang, J. & Mei, J. Topological valley-chiral edge states of lamb waves in elastic thin plates. *Appl. Phys. Express* **11**, 057302 (2018).
111. Zhu, H., Liu, T.-W. & Semperlotti, F. Design and experimental observation of valley-hall edge states in diatomic-graphene-like elastic waveguides. *Phys. Rev. B* **97**, 174301 (2018).
112. Zhu, H. et al. Observation of chiral phonons. *Science* **359**, 579–582 (2018).
113. Zhang, T. et al. Double-weyl phonons in transition-metal monosilicides. *Phys. Rev. Lett.* **120**, 016401 (2018).
114. Liu, D. & Shi, J. Circular phonon dichroism in weyl semimetals. *Phys. Rev. Lett.* **119**, 075301 (2017).
115. Zhang, L., Ren, J., Wang, J.-S. & Li, B. Topological nature of the phonon hall effect. *Phys. Rev. Lett.* **105**, 225901 (2010).
116. Li, S., Zhao, D., Niu, H., Zhu, X. & Zang, J. Observation of elastic topological states in soft materials. *Nat. Commun.* **9**, 1370 (2018).
117. Serra-Garcia, M. et al. Observation of a phononic quadrupole topological insulator. *Nature* **555**, 342 (2018).
118. Wang, M., Ye, L., Christensen, J. & Liu, Z. Valley physics in non-hermitian artificial acoustic boron nitride. *Phys. Rev. Lett.* **120**, 246601 (2018).

## Acknowledgements

X.J.Z. and L.M.H. are supported by the National Natural Science Foundation of China (Grant No. 11625418 and No. 51732006). M.X. is supported by the U. S. National Science Foundation (Grant No. CBET-1641069). Y.C. acknowledges the support from the National Natural Science Foundation of China (NSFC) (Grant Nos. 11834008, 11874215, 11674172, and 11574148) and from the National Basic Research Program of China (Grant No. 2017YFA0303702). J.C. acknowledges the support from the European Research Council (ERC) through the Starting Grant No. 714577 PHONO-META and from the MINECO through a Ramón y Cajal grant (Grant No. RYC-2015-17156).

## Author contributions

All authors contributed equally to this work.

## Additional information

**Competing interests:** The authors declare no competing interests.

**Reprints and permission** information is available online at <http://npg.nature.com/reprintsandpermissions/>

**Publisher's note:** Springer Nature remains neutral with regard to jurisdictional claims in published maps and institutional affiliations.



**Open Access** This article is licensed under a Creative Commons Attribution 4.0 International License, which permits use, sharing, adaptation, distribution and reproduction in any medium or format, as long as you give appropriate credit to the original author(s) and the source, provide a link to the Creative Commons license, and indicate if changes were made. The images or other third party material in this article are included in the article's Creative Commons license, unless indicated otherwise in a credit line to the material. If material is not included in the article's Creative Commons license and your intended use is not permitted by statutory regulation or exceeds the permitted use, you will need to obtain permission directly from the copyright holder. To view a copy of this license, visit <http://creativecommons.org/licenses/by/4.0/>.

© The Author(s) 2018